

# Frustum pyramid shape of indium bump to lengthen cycling life of InSb infrared detector

Xiaoling Zhang<sup>1</sup> · Yanping Gao<sup>1</sup> · Qingduan Meng<sup>1,2</sup> · Yanqiu Lv<sup>2</sup> · Junjie Si<sup>2</sup>

Received: 5 December 2016 / Accepted: 30 January 2017 / Published online: 3 February 2017  
© Springer Science+Business Media New York 2017

**Abstract** The thermal deformation appearing in indium antimonide infrared focal plane arrays (InSb IRFPAs) subjected to thermal shock tests, will easily incur the fracture of InSb chip, this phenomenon restricts the final yield of InSb IRFPAs. In light of the proposed equivalent method, the three dimensional structural modeling of InSb IRFPAs is developed, and the simulated strain distributions are consistent with the buckling pattern, the shallow groove and the local flatness, appearing on the top surface of InSb IRFPAs at the corresponding regions. After comparing the deformation profiles at different regions, we deduce that the top surface flatness of InSb IRFPAs will be improved with frustum pyramid indium bump arrays, and this deduction is verified by the subsequent simulation results. That is, when the top surface area of indium bump is smaller than its bottom surface area, in this paper, the diameter of indium bump bottom surface is set with 24  $\mu\text{m}$ , the simulated Z-components of strain is uniformly covering the whole top surface of InSb IRFPAs, and the deformation amplitude is decreased slowly with the decreasing top surface area of indium frustum pyramid arrays. These findings are beneficial to further improve the flatness of InSb IRFPAs, correspondingly, to lengthen its temperature cycling life.

**Keywords** InSb · Infrared focal plane arrays · Thermal deformation · Indium frustum pyramid

## 1 Introduction

Infrared focal plane arrays (IRFPAs) detectors, active in 3–5  $\mu\text{m}$  range, have been widely used in military fields, such as ballistic missile defense system, infrared imaging missile system, and military remote-sensing satellite (Tidrow and Dyer 2001; Qiu et al.

---

✉ Qingduan Meng  
qdmengly@163.com

<sup>1</sup> School of Information Engineering, Henan University of Science and Technology, Luoyang 471023, China

<sup>2</sup> Academy Key Laboratory of Science and Technology on Infrared Detector, Luoyang 471009, China

2015; Hu et al. 2016). For the existing well-developed IRFPAs detectors, indium antimonide (InSb) IRFPAs have excellent uniformity in the middle wavelength range, and mercury cadmium telluride (HgCdTe) IRFPAs occupy a dominant position in dual or multiband detector fields (Rogalski 2012). Compared with HgCdTe IRFPAs, the production process of InSb IRFPAs has a higher maturity and an excellent uniformity. For example, the highest mass production rate, exceeding 3000 InSb sensor chip assemblies per year, was held by Raytheon Company. Besides, Raytheon Company delivered the largest format InSb IRFPAs of  $4\text{ k} \times 4\text{ k}$  arrays in 2009 (Hoffman et al. 2004a, b). However, for the large format IRFPAs, the fracture of InSb chip in thermal shock tests, limits its final yield, and has been a major problem in the mass production. All these phenomena originate from its special structure and its low temperature operation environment. InSb IRFPAs is usually fabricated by flip chip bonding technology. That is, indium bumps are formed firstly on both the InSb chip and the silicon readout integrated circuits (silicon ROIC), then both the InSb chip and the silicon ROIC are aligned and force is applied to cause the indium bumps to cold-weld together. Here, the temperature of flip chip process is 370 K, and the applied force is 30 N. After that, the InSb chip is back thinned to less than one diffusion length for higher quantum efficiency. Taking account of the maturity of thinning process, the InSb chip is usually thinned to three times diffusion length, about  $10\text{ }\mu\text{m}$  (Hoffman et al. 2004a, b).

To achieve a high signal-to-noise ratio, InSb IRFPAs usually operate at liquid nitrogen temperature (77 K). When the temperature of InSb IRFPAs rapidly reduces from room temperature to 77 K, because of the large coefficient of thermal expansion (CTE) mismatch between the neighboring parts, the accumulated thermal strain is a major cause to incur the fracture of InSb chip, especially in large format InSb IRFPAs (Merrill et al. 2004).

To improve the reliability of hybrids IRFPAs assembly, the balanced composite structure is employed to prevent the bending of IRFPAs, which is attached to the backside of the silicon ROIC with suitable thickness and suitable composition (Merrill et al. 2004; Finger et al. 2005). Furthermore, in L-3 Cincinnati Electronics, the front side illuminated and the reticulated pixel structure is developed to eliminate the amassed thermal strain in the temperature cycling tests (Davis and Greiner 2011). In these delivered reports, the research groups pointed out that the flatness of IRFPAs at room temperature is a key factor to determine the stress level built in the IRFPAs. Furthermore, they also pointed out that the temperature cycling life of the IRFPAs will continue to increase to a higher number, in light of the redesign and the optimization of the indium bump processes (Davis and Greiner 2011).

In our previous research, the three dimensional structural modeling of InSb IRFPAs is created and verified by the crack originating sites, the crack distribution and the global buckling pattern presenting on the fragmented top surface of InSb IRFPAs, respectively. The simulated Z-components of strain distribution are identical with the photograph of InSb IRFPAs taken at room temperature (Meng et al. 2012a, b; Zhang et al. 2013, 2014a, b, 2015). Inspired by the fragmentary description of the IRFPAs with a longer temperature cycling life, and basing on the facts that the simulated Z-components of strain distribution is consistent with the photograph of InSb IRFPAs taken at room temperature (Meng et al. 2012a, b; Zhang et al. 2013, 2014a, b), after comparing the deformation profiles presenting on the whole top surface of InSb IRFPAs at different regions, we deduce that the top surface flatness of InSb IRFPAs will be improved with frustum pyramid indium bump arrays, and this deduction is verified by both the subsequent simulation results and the experimental results provided by other research groups. This research is

beneficial to explore the optimization direction of indium bump arrays, and to improve the temperature cycling life of IRFPAs without cracks generated in thermal shock tests.

## 2 InSb IRFPAs structure and deformation distribution characteristic

The InSb IRFPAs is composed of three layers, including the upper InSb photosensitive layer, the bottom silicon ROIC and the intermediate interconnecting layer, made of the indium bump arrays and the reticular underfill (Rogalski 2012).

To obtain a high signal-to-noise ratio, the InSb IRFPAs operates at liquid nitrogen temperature (77 K). When its temperature rapidly decreases from 300 to 77 K, the amassed thermal strain and stress cause the fracture of InSb chip, the typical fracturing photograph of InSb IRFPAs is shown in Fig. 1a. For easy comparison of the deformation distribution, here, the typical photograph of InSb IRFPAs without cracks is shown in Fig. 1b. According to the typical deformation photographs shown in Fig. 1, we draw the following deformation distribution characteristics. That is, the InSb chip touching with the indium bump arrays is upwardly convex, and the InSb chip touching with the underfill is downwardly concave. The convex region alternates with the concave region, and their areas are comparable. Clearly, this is a typical square checkerboard buckling pattern. On the upper side of the InSb IRFPAs photographs, its surface is flat, and the square checkerboard buckling pattern appearing in the center part of the InSb IRFPAs vanishes.

## 3 Modeling creation and parameters selection

The structure of InSb IRFPAs is complex, and its characteristic size ranges in scale from the micrometer to the millimeter. Therefore, in the structural modeling of InSb IRFPAs, a large number of elements are needed to mesh the whole structure, which causing the stiffness matrix of InSb IRFPAs in ANSYS is too large to be solved. To overcome this

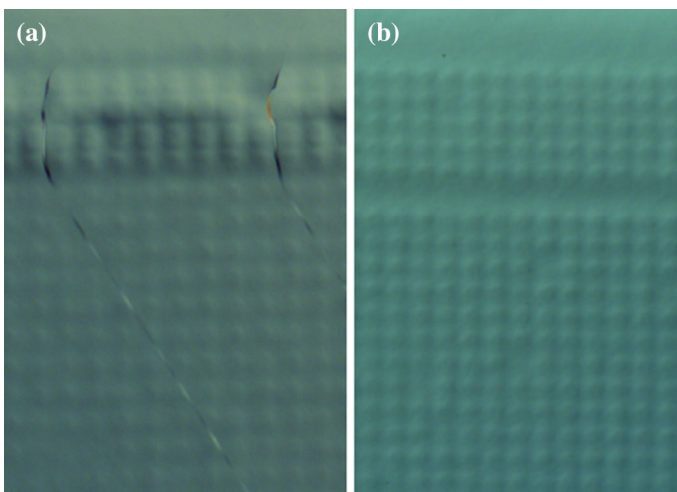


**Fig. 1** Typical photographs of InSb IRFPAs taken at room temperature, **a** InSb IRFPAs with cracks, **b** InSb IRFPAs without crack

problem, an equivalent modeling was proposed in the reference (Meng et al. 2012a, b) and the reference (Zhang et al. 2014a, b), where, a smaller arrays is employed to replace the larger arrays for creating the three dimensional modeling of InSb IRFPAs.

Due to the CTE mismatch between the InSb chip and the silicon ROIC, the indium bumps experience stress from the thermal cycling between 300 and 77 K. These thermal cycles produce the relative displacement between the InSb chip and the silicon ROIC, and results in shear stress at the interfaces between the indium bump and the metal pad. The displacement ( $\Delta L$ ) indium bumps experience is represented as (Jiang et al. 2004)

$$\Delta L = L_0 \Delta T (\alpha_{FPA} - \alpha_{Si}), \quad (1)$$

where  $L_0$  is the distance from the indium joint to the center point of IRFPAs hybrid, which is treated as a neutral point, where no relative displacement exists between the silicon ROIC and the InSb chip. Both  $\alpha_{FPA}$  and  $\alpha_{Si}$  are the CTE of the InSb chip and the silicon ROIC, respectively.  $\Delta T$  is the temperature change range. When the temperature change range is fixed, the displacement indium bumps experience under thermal shock tests is proportional to the product of both  $L_0$  and  $(\alpha_{FPA} - \alpha_{Si})$ . In  $128 \times 128$  InSb IRFPAs, there are 16,384 indium bumps situating in the  $128 \times 128$  square matrix. Because of the geometrical symmetry, only one-eighth of the overall package is modeled in ANSYS, which contains 2080 indium bumps, these indium bumps distribute in the equilateral triangle sub-matrix. In the proposed equivalent method, the block composed with the neighboring  $4 \times 4$  InSb photosensitive units is replaced by one InSb photosensitive unit with twice linear coefficient of thermal expansion in both the vertical and the horizontal directions. Thus the real displacements in the large format are substituted with the equivalent displacements calculated in the small format with a large thermal mismatch. In the equivalent modeling of InSb IRFPAs, there are 276 indium bumps distributing uniformly in the equilateral triangle sub-matrix, just as shown in Fig. 2. In the equivalent modeling of InSb IRFPAs, InSb chip dimensions are  $2500 \mu\text{m} \times 2500 \mu\text{m} \times 10 \mu\text{m}$ , and attached to silicon ROIC substrate with  $46 \times 46$  indium bumps arrays, silicon ROIC substrate dimensions are  $3200 \mu\text{m} \times 3200 \mu\text{m} \times 300 \mu\text{m}$ . The height of indium bump arrays is set at  $10 \mu\text{m}$  with  $50 \mu\text{m}$  pitch, and its bottom surface diameter is set with  $24 \mu\text{m}$ , its top surface diameter increases from 6 to  $36 \mu\text{m}$  in step of  $6 \mu\text{m}$  in the simulation. In the surrounding of indium bump arrays, underfill is filled between the InSb chip and the silicon ROIC, its dimensions are  $2500 \mu\text{m} \times 2500 \mu\text{m} \times 10 \mu\text{m}$ .

The CTEs of materials are strongly dependent on the temperature, usually decreases with the decreasing temperature. In order to calculate exactly the accumulated thermal strain in the layered structure, in this paper, the employed CTE models are all temperature-dependent. Both the silicon ROIC and the negative electrode are homogeneous and isotropic linear elastic materials. InSb is an anisotropic linear elastic material. The indium bump is a viscoplastic material, its Young's modulus increases with the decreasing temperature. The underfill is a viscoelastic material in its glass transmitting region, once cured

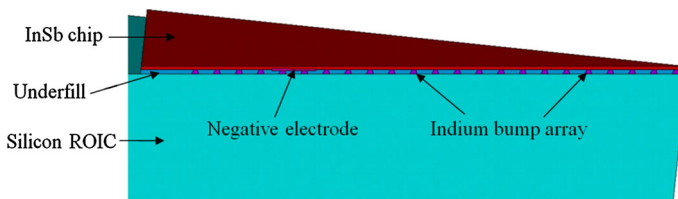
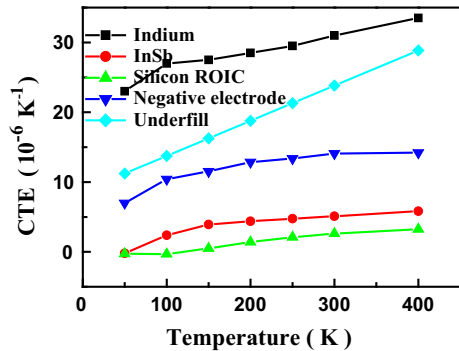


**Fig. 2** Three dimensional modeling of InSb IRFPAs

**Fig. 3** Coefficients of thermal expansion depending on temperature for InSb, indium bumps, underfill, negative electrode and silicon ROIC



completely, becomes a linear elastic material. The CTEs of materials in InSb IRFPAs are plotted in Fig. 3 (He et al. 2000; White and Collins 1972; Cheng et al. 2012; Chang and Patrick 2009; Gibbons 1958; Okada and Tokumaru 1984).

In the simulation, the initial temperature is set at 370 K. At this temperature, the underfill is cured, and its volume shrinkage is about 4%. After that, InSb IRFPAs is cooled naturally down to room temperature.

InSb is a brittle material with a cubic symmetry, i.e., a lattice of zinc blend structure. Because of the cubic crystal lattice, the material is stiffer in some directions and more compliant in other directions (Pandolfi and Weinberg 2011). Inside InSb chip, its thickness is only 10  $\mu\text{m}$ , and there are four parallel or vertical isolation troughs around every mesa-junction with depth about 2–4  $\mu\text{m}$ . Besides, both median cracks (3–4  $\mu\text{m}$ ) and lateral cracks (1–2  $\mu\text{m}$ ) may appear in the backside thinning process of InSb IRFPAs (Wasmer et al. 2008). All these factors will weaken the toughness of InSb chip along its normal direction. In order to assess the damage degree of the InSb chip, generated in its surface fabrication process, its out-of-plane elastic modulus is set from 10 to 100% Young's modulus of its bulk material, which corresponds to severely damaged and no damaged InSb chip in the normal direction (Hauck et al. 2005). In our previous research, we found that when the out-of-plane elastic modulus of InSb chip is set to be 30% its Young's modulus, the simulated maximum Von Mises stress appearing on the top surface of InSb IRFPAs are in good agreement with the fracture origination zone and the crack distribution in the fracture photographs (Meng et al. 2012a, b), and the Z-components of strain appearing on the top surface of InSb IRFPAs are also identical with the scenario of InSb IRFPAs under thermal shock tests (Meng et al. 2012a, b).

All the employed mechanical property parameters are listed in Table 1. Where E is the Young's modulus,  $\mu$  is the Poisson's ratio. In the temperature range from 50 to 370 K, the linear thermal expansion coefficient of underfill  $\alpha$  can be approximated by He et al. (2000)

$$\alpha = 22.46 \times 10^{-6} + 5.04 \times 10^{-8} \times (T - 273), \quad (2)$$

where T is in kelvin.

## 4 Results

The top surface profile of InSb IRFPAs is clearly displayed in Fig. 1, and this is the only directly observed deformation distribution photographs taken at room temperature with the help of graphic microscope. In ANSYS simulation results, these deformation distribution

**Table 1** Elastic material parameters at different temperatures

Materials	Elastic modulus (E/GPa)	Poisson's ratio ( $\mu$ )	Temperatures (T/K)
Si ROIC	163	0.28	77–370
InSb chip	409 (in plane) 123 (out of plane)	0.35	77–370
Indium bump	20.54	0.4326	76
	16.24	0.4408	187
	12.70	0.4498	370
Underfill	0.0002/ $\alpha$	0.30	77–370
Negative electrode	79	0.44	77–370

characteristics are described by Z-components of strain. So in this paper, we employ the Z-components of strain to assess the effects of indium bump shapes on the deformation degree of InSb IRFPAs.

Employing the three dimensional modeling prescribed in the former section, we obtained the simulated top surface profile of InSb IRFPAs, just as shown in Fig. 4. Firstly, in the center part of InSb IRFPAs top surface, the InSb chip touching with the indium bump arrays is convex upwards, and the InSb chip touching with the underfill is concave downwards, the convex regions alternate with the concave zones, and their areas are comparable. This typical square checkerboard buckling pattern is well identical to the deformation distribution photographs shown in Fig. 1. Secondly, around the center photosensitive cell arrays, where the negative electrode was placed beneath the InSb photosensitive layer, a shallow groove appears on the top surface of InSb IRFPAs. This local deformation distribution characteristic is also well in agreement with that appearing in Fig. 1b, at the corresponding regions. Thirdly, at the outer edge of InSb IRFPAs, where the indium bump arrays does not exist, the underfill fills up the gap between the InSb photosensitive layer and the silicon ROIC, the top surface of InSb IRFPAs is flat. This deformation characteristic agrees with the deformation characteristics shown in the upper side of Fig. 1. In one word, the simulated Z-components strain distribution contains all the deformation features appearing in the photograph of InSb IRFPAs taken at room temperature.

**Fig. 4** Simulated deformation distribution of the whole InSb IRFPAs at room temperature, in which the shape of indium bumps is cylinder, and its diameter is set with 24  $\mu\text{m}$

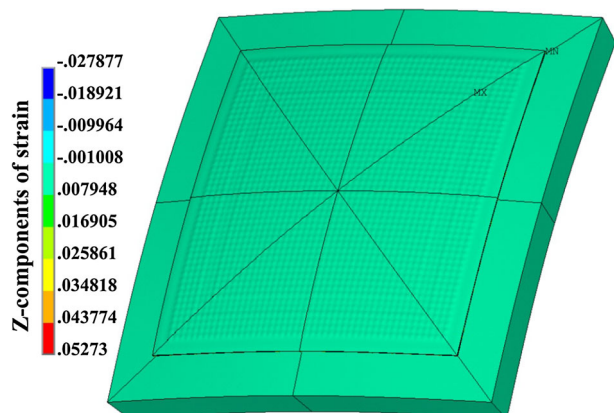
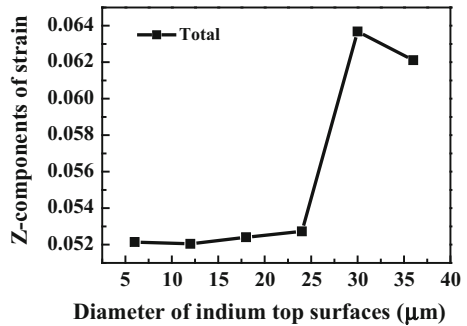


**Fig. 5** Simulated maximum Z-components of strain of InSb IRFPAs as a function of the diameter of indium bump top surface, here the diameter of indium bump bottom surface is fixed with 24  $\mu\text{m}$



According to the fabrication process of InSb IRFPAs, we consider that the chemical shrinkage appearing in the curing process of underfill is the origination of the surface deformation, the deformation amplitude will increase with the decreasing temperature, and the convex and concave deformation distribution is determined by the structural design of the intermediate layer composed by the indium bump arrays and the underfill.

In the modeling of InSb IRFPAs in Fig. 4, the diameter of indium bump is set as 24  $\mu\text{m}$  with 50  $\mu\text{m}$  pitch. Taking account of the deformation distribution characteristic at the outer edge of InSb IRFPAs top surface, where the indium bump arrays do not exist, no periodical rising and falling exists. At the same time, in the center part of the InSb IRFPAs top surface, the InSb chip touching with the underfill is concave downwards, and the height of the valley bottom is approaching the height of the outer edge of InSb IRFPAs. Besides, we noticed that, on the top surface of InSb IRFPAs, the InSb chip touching with the indium bump arrays is the only part convex upwards. Basing on all these information, we infer that once the touching area between the InSb chip and the indium bump is reduced, the deformation amplitude appearing on the top surface of InSb IRFPAs will decrease, and the peak-to-valley flatness of InSb IRFPAs will be improved.

In order to learn the effect from the touching area between the InSb chip and the indium bump on the deformation amplitude appearing on the InSb IRFPAs top surface, here the diameter of the indium bump top surface is decreased from 36 to 6  $\mu\text{m}$  in step of 6  $\mu\text{m}$ , and the diameter of the indium bump bottom surface is kept with 24  $\mu\text{m}$ , and all the other structure sizes remain unchanged. The simulated maximal Z-components of strain are plotted in Fig. 5. Apparently when the diameter of the indium top surface reduces from 36 to 6  $\mu\text{m}$ , the simulated Z-components of strain shows the typical characteristic of a piecewise function. When the diameter of the indium top surface is larger than 24  $\mu\text{m}$ , the maximal Z-components of strain keeps at a larger value, which fluctuates at 0.062, and when the diameter of indium top surface is smaller than 24  $\mu\text{m}$ , the maximal Z-components of strain seems to decrease slowly.

## 5 Discussion

In order to compare the deformation distribution appearing on the top surface of InSb IRFPAs, here we select two diameters of indium top surface with 36 and 12  $\mu\text{m}$ , and the simulated Z-components of strain are shown in Figs 6 and 7, respectively. It is necessary to point out that in all these simulation results, the only changed structural size is the diameter

**Fig. 6** Simulated deformation distribution of the whole InSb IRFPAs, in which the diameter of indium bump *top* surface is set with  $36\ \mu\text{m}$ , and its *bottom* surface diameter is set with  $24\ \mu\text{m}$

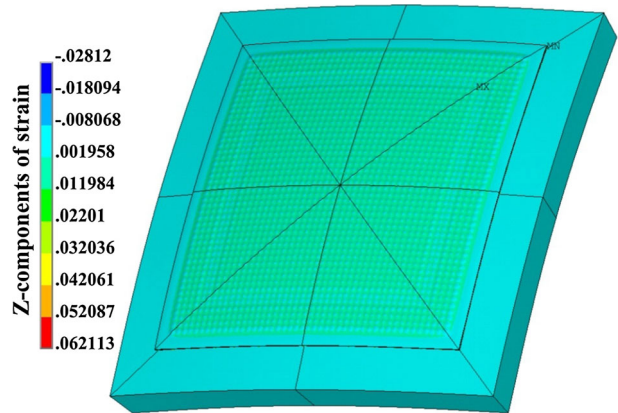
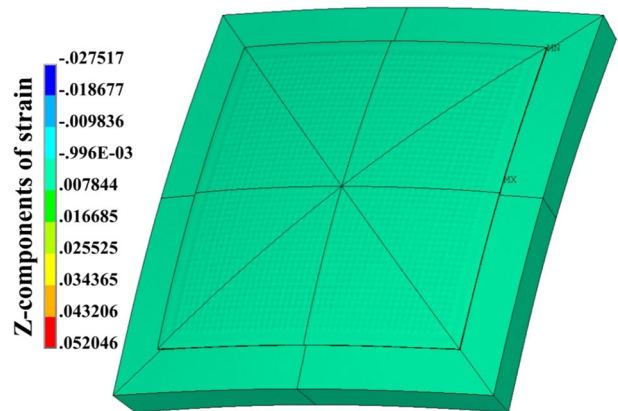


**Fig. 7** Simulated deformation distribution of the whole InSb IRFPAs, in which the diameter of indium bump *top* surface is set with  $12\ \mu\text{m}$ , and its *bottom* surface diameter is set with  $24\ \mu\text{m}$



of the indium top surface. Correspondingly, the underfill surrounding the indium bump arrays is also changed. But the total thickness of the InSb IRFPAs and the thickness of each layer in the InSb IRFPAs do not change with the variable shapes of the indium bump arrays. Because all the simulated structures have the same thickness, the Z-components of strain can be employed directly to assess the deformation degree of InSb IRFPAs.

When the diameter of the indium bump top surface is set with  $36\ \mu\text{m}$ , the simulated Z-components of strain distribution are shown in Fig. 6, and the maximal Z-components of strain are 0.062. Apparently, in InSb photosensitive cell arrays, the typical square checkerboard buckling pattern is clear, and the Z-components of strain mean value is about 0.022, this value is obviously larger than 0.0020, a Z-components of strain value appearing in the region surrounding the InSb photosensitive cell arrays.

When the diameter of the indium bump top surface is set with  $12\ \mu\text{m}$ , the simulated Z-components of strain distribution are shown in Fig. 7, and the maximal Z-components of strain are 0.052. Apparently, on the whole top surface of InSb IRFPAs, the Z-components of strain is uniform, and the square checkerboard buckling pattern is fuzzy and indistinct, the flatness of InSb IRFPAs is in the range of  $-0.001$  to  $0.008$ , a numerical range presented in the contour of Z-components of strain. Up to present, we consider that once the diameter of indium bump top surface is smaller than  $24\ \mu\text{m}$ , the maximal Z-components of strain



appearing on the top surface of InSb IRFPAs fluctuate at 0.0523, and decrease slowly with the decreasing indium bump top surface diameter, the buckling amplitude is also decreased slowly with the decreasing indium bump top surface diameter. In this situation, the flatness of InSb IRFPAs is in an acceptable range.

We noticed that frustum pyramid shape of indium bump have been employed in several large format IRFPAs fabricated in Rockwell or in Raytheon (Rogalski 2012; Norton 2002). And these large format IRFPAs have experienced several thousand cool down cycles. Up to now, we conclude that the flatness of IRFPAs will be improved with frustum pyramid indium arrays, and this indium bump shape is beneficial to lengthen its temperature cycling life.

## 6 Conclusions

Basing on the facts that the simulated Z-components of strain distribution is identical with the photograph of the typical InSb IRFPAs, at every corresponding regions, and after analyzing the deformation features on the different regions of InSb IRFPAs, we infer that the flatness of InSb IRFPAs is determined by the shape of the indium bump arrays, this conclusion is verified by the subsequent simulation results. When the shape of the indium bump arrays is processed with frustum pyramid, the Z-components of strain on the top surface of InSb IRFPAs is uniform, and both the maximal Z-components of strain and the buckling amplitude decrease slowly with the decreasing indium top surface diameter. These findings will supply a new approach to improve the reliability of the InSb IRFPAs, and to lengthen its temperature cycling life.

**Acknowledgements** The research was supported by the Young Scientists Fund of the National Natural Science Foundation of China (Grant No. 61505048) and by the Aero Science Foundation of China (Grant No. 20152442001).

## References

- Chang, R.W., Patrick, M.F.: Constitutive relations of indium in extreme temperature electronic packaging based on Anand model. *J. Electron. Mater.* **38**, 1855–1859 (2009)
- Cheng, X., Liu, C., Silberschmidt, V.V.: Numerical analysis of thermo-mechanical behavior of indium micro joint at cryogenic temperatures. *Comput. Mater. Sci.* **52**, 274–281 (2012)
- Davis, M., Greiner, M.: Indium antimonide large-format detector arrays. *Opt. Eng.* **50**, 061016–1–061016–7 (2011)
- Finger, G., Dorn, R.J., Meyer, M., Mehrgan, L., Stegmeier, J., Moorwood, A.: Hybrid active pixel sensors in infrared astronomy. *Nucl. Inst. Methods Phys. Res. A* **549**, 79–86 (2005)
- Gibbons, D.F.: Thermal expansion of some crystals with the diamond structure. *Phys. Rev.* **112**, 136–140 (1958)
- Hauck T., Bohm C., Muller W.H.: Weibull statistics of silicon die fracture. In: Proceedings of the European SimE, Berlin, Germany, vol. 18–20, pp. 242–247 (2005)
- He, Y., Moreira, B.E., Overson, A., Nakamura, S.H., Bider, C., Briscoe, J.F.: Thermal characterization of an epoxy-based underfill material for flip chip packaging. *Thermochim. Acta* **357–358**, 1–8 (2000)
- Hoffman, A.W., Corrales, E., Love, P.J., Rosbeck, J.P., Fowler, A.M., et al.:  $2\text{ K} \times 2\text{ K}$  InSb for astronomy. *Proc. SPIE* **5499**, 59–67 (2004a)
- Hoffman, A.W., Love, P.L., Rosbeck, J.P.: Mega-pixel detector arrays: visible to  $28\ \mu\text{m}$ . *Proc. SPIE* **5167**, 194–203 (2004b)
- Jiang, J., Tsao, S., O'Sullivan, T., Razeghi, M., Brown, G.J.: Fabrication of indium bumps for hybrid infrared focal plane array applications. *Infrared Phys. Technol.* **45**, 143–151 (2004)

- Meng, Q.D., Yu, Q., Zhang, L.W., Lv, Y.Q.: Mechanical parameters selection in InSb focal plane array detector normal direction. *Acta Phys. Sin.* **61**, 226103–1–226103–5 (2012a)
- Meng, Q.D., Zhang, X.L., Zhang, L.W., Lv, Y.Q.: Structural modeling of  $128 \times 128$  InSb focal plane array detector. *Acta Phys. Sin.* **61**, 190701–1–190701–6 (2012b)
- Merrill, K.M., Fowler, A., Ball, W., Henden, A., Vrba, F., McCreight, C.R.: Orion II: the second-generation readout multiplexer for the largest infrared hybrid focal plane. *Proc. SPIE* **5167**, 186–193 (2004)
- Norton, P.: HgCdTe infrared detectors. *Opto-Electron. Rev.* **10**, 159–174 (2002)
- Okada, Y., Tokumaru, Y.: Precise determination of lattice parameter and thermal expansion coefficient of silicon between 300 and 1500 K. *J. Appl. Phys.* **56**, 314–320 (1984)
- Pandolfi, A., Weinberg, K.: A numerical approach to the analysis of failure modes in anisotropic plates. *Eng. Fract. Mech.* **78**, 2052–2069 (2011)
- Qiu, W., Hu, W.: Laser beam induced current microscopy and photocurrent mapping for junction characterization of infrared photodetectors. *Sci. China Phys. Mech. Astron.* **58**(2), 027001–1–027001–13 (2015)
- Rogalski, A.: Progress in focal plane array technologies. *Prog. Quantum Electron.* **36**, 342–473 (2012)
- Tidrow, M.Z., Dyer, W.R.: Infrared sensors for ballistic missile defense. *Infrared Phys. Technol.* **42**, 333–336 (2001)
- Wasmer, K., Ballif, C., Pouvreau, C., Schulz, D., Michler, J.: Dicing of gallium-arsenide high performance laser diodes for industrial applications part I. scratching operation. *J. Mater. Process. Technol.* **198**, 114–121 (2008)
- Weida, H., Jian, L., Fangyu, Y., Xiaoshuang, C., Wei, L.: Recent progress of subwavelength photon trapping HgCdTe infrared detector. *J. Infrared Millim. Waves* **35**, 25–36 (2016)
- White, G.K., Collins, J.G.: Thermal expansion of copper, silver, and gold at low temperatures. *J. Low Temp. Phys.* **7**, 43–75 (1972)
- Zhang, X.L., Meng, Q.D., Yu, Q., Zhang, L.W., Lv, Y.Q.: Thermal buckling analysis in InSb focal plane array detector. *J. Mech. Sci. Technol.* **27**, 1809–1813 (2013)
- Zhang, X.L., Meng, Q.D., Zhang, L.W., Lv, Y.Q.: Modeling and deformation analyzing of InSb focal plane arrays detector under thermal shock. *Infrared Phys. Technol.* **63**, 28–34 (2014a)
- Zhang, X.L., Meng, Q.D., Zhang, L.W., Lv, Y.Q.: Negative electrode structure design in InSb focal plane array detector for deformation reduction. *J. Mech. Sci. Technol.* **28**, 2281–2285 (2014b)
- Zhang, X.L., Meng, Q.D., Zhang, L.W.: Dependence of the deformation of  $128 \times 128$  InSb focal-plane arrays on the silicon readout integrated circuit thickness. *Open Elect. Electron. Eng. J.* **9**, 170–174 (2015)